Contents lists available at ScienceDirect

International Journal of Multiphase Flow

Surface and internal gravity waves on a viscous liquid layer: Initial-value problems

Ramana Patibandla [a], Saswata Basak [b], Ratul Dasgupta [b], Anubhab Roy [a],*

[a] *Department of Applied Mechanics, Indian Institute of Technology Madras, Chennai, 600036, India*
[b] *Department of Chemical Engineering, Indian Institute of Technology Bombay, Mumbai 400 076, India*

ARTICLE INFO

ABSTRACT

We study a class of initial value problems (IVPs) involving perturbations on a density stratified, quiescent, viscous liquid layer with a free-surface. The geometry is a two-dimensional, rectangular configuration taking into account surface-tension and gravity. Linearised predictions are obtained by solving the IVP analytically for free-surface and vortical initial perturbations. The viscous spectrum comprises a discrete spectrum of propagating surface and internal modes and damped vorticity modes. Continuous spectra may also exist depending on whether the domain is bounded or unbounded. It is shown that independent of stratification, the vorticity modes in the spectrum play an important role. For an unstratified pool of a highly viscous liquid, the vorticity modes are found to make a large contribution to the temporal evolution of the transient vorticity layer, at the free-surface. It is demonstrated that the temporal evolution of localised vortical perturbations sufficiently deep inside the pool, cannot be captured by surface modes (capillarity–gravity modes) and require contributions from the vorticity modes. The free-surface signature of a deep, localised, vortical perturbation is however found to be negligible. On a stratified pool of viscous liquid, such vortical initial perturbations are shown to have significant projections on vorticity as well as internal gravity modes. In the infinite depth limit of an unstratified pool, the contribution from the continuous spectrum vorticity modes is analysed vis-a-vis that from their finite depth, discrete spectrum counterparts. Several analytical predictions are compared against direct numerical simulations (DNS) obtaining excellent agreement. Our results extend classical ones due to Lamb (1932), Yih (1960), Prosperetti (1976) and Prosperetti and Cortelezzi (1982) and receive support from nonlinear simulations.

1. Introduction

Solution to initial value problems (IVPs) for surface waves on a quiescent or sheared liquid layer have remained an active topic of research since the classical analysis by Cauchy (1827) and Poisson (1818), see Ellingsen (2014), Shardt et al. (2016), Shen et al. (2017, 2018) and Tyvand et al. (2021a,b). For an unstratified, quiescent layer modelled as being infinitely deep, this was first done in the linearised, inviscid-irrotational framework (also known as the pebble in the pond problem, see Lamb (1932), Debnath (1994) and Craik (2004)). For a given initial perturbation, the interface shape and perturbation velocity potential at any later time may be expressed as inverse Fourier (Hankel) integrals over initial conditions weighted by a harmonic time dependence, the frequency of which comes from the dispersion relation (Debnath, 1994). While such integrals can now be solved numerically quite routinely (see generated using Mathematica Wolfram, 2013), their physical content becomes clear from the application of method of stationary phase (see sec. 2.1.3 in Johnson (1997)) leading

to the notion of a local Fourier mode, whose envelope propagates at the group velocity.

Inclusion of viscosity into the analysis using a monochromatic Fourier mode was first reported by Basset (1888) and subsequently by Lamb (1932) and Harrison (1908) who obtained the viscous dispersion relation for surface waves on a quiescent, unstratified pool of infinite and finite depth. Lamb (1932) also commented on the continuous spectrum of eigenmodes for an infinitely deep pool of viscous liquid. An explicit solution to the linearised, viscous initial-value problem for a localised surface deformation on an infinitely deep, cylindrical pool was reported by Miles (1968). Using Hankel transform (in radial direction) and Laplace transform (in time), Miles (1968) obtained the solution to the viscous (linearised) Cauchy–Poisson problem comprising a free-surface displacement and a surface impulse. In rectangular geometry, the initial value problem for pure surface deformation (single Fourier mode), as well as a combination of surface

---

(a) $t = 0$ s

(b) $t = 15$ s
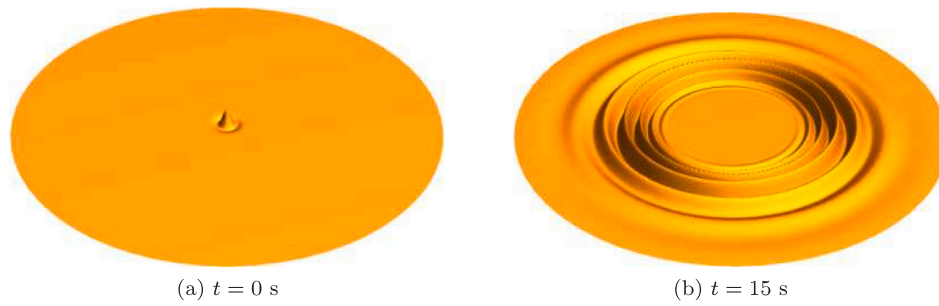
Fig. 1. Three dimensional rendering of axisymmetric surface gravity waves from the inviscid, Cauchy–Poisson solution (a) The initial surface perturbation (Miles, 1968) is $\eta(r, 0) = 40 \left(1 - r^2\right) \exp\left(-r^2\right)$ on a quiescent pool of infinite depth. Panel (b) At any time $t > 0$, the interface shape is represented by Debnath (1994) $\eta(r, t) = \int_0^\infty dk \, k J_0(kr) \mathbb{H}(\eta(r, 0)) \cos(\sqrt{gkt})$ where $\mathbb{H}(f(r))$ is the 0th order Hankel transform of $f(r)$.

Table 1
A representative summary of literature.

No.	Type	Reference	Type	Visc./Invisc	Remarks
1		Wu and Mei (1967)	IVP	2D, Inviscid	Point source starting at $t = 0$. A free surface is also considered.
2		Thomas and Stevenson (1972)	Sim. sol.	2D, Viscous	Oscillating localised disturbance (similarity solution). Experimentally verified
3		Debnath and Guha (1989)	IVP	2D, Inviscid	Axisymmetric Cauchy–Poisson problem
4	Stratified	Rollins and Debnath (1992)	IVP	2D, Inviscid	Axisymmetric, rotating, Cauchy–Poisson problem
5		Voisin (1991)	IVP	3D, Inviscid	Monochromatic and impulsive point sources. Oscillations of a sphere.
6		Simakov (1993)	IVP	3D, Inviscid	Impulsive point source. Simple extended source.
7		Voisin (1994)	IVP	3D , Inviscid	Moving point source: oscillating and non-oscillating
8		Lighthill (1996)	IVP	3D, Inviscid	Initial localised disturbance. Effect of viscosity.
9		Ghosh et al. (2000)	IVP	2D, Inviscid	Finite depth, inertial surface
10		Gurski et al. (2004)	Normal mode	3D, Viscous	Proved that a countably infinite spectrum of non-oscillatory modes exist
11		Cauchy (1827) & Poisson (1818)	IVP	2D, Inviscid	A spectrum of modes on a non-quiescent free-surface as initial data.
12		Basset (1888)	Normal Mode	2D, Inviscid	Finite depth
13		Lamb (1932)	Normal Mode	2D, Viscous	Continuous spectrum for infinite depth
14	Unstratified	Harrison (1908) and Lamb (1932)	Normal Mode	2D, Viscous	Bottom layer is considered as infinite depth.
15		Prosperetti (1976)	IVP	2D, Viscous	Derive an integro-differential amplitude equation for the free-surface.
16		Prosperetti (1981)	IVP	3D, Viscous	Two-fluid; Derive an integro-differential amplitude equation for the interface.
17		Prosperetti and Cortelezzi (1982)	IVP	3D, Viscous	Finite Depth; Derive an integro-differential amplitude equation for the free-surface for a Dirac-delta vortical disturbance.
18		Antuono and Colagrossi (2013)	Normal Mode	2D, Viscous	Approximate formula for damping rates of viscous gravity waves.
19		Denner (2016)	IVP	2D, Viscous	Small amplitude pure capillary waves on a free-surface
20		Vartdal and Osnes (2019)	IVP	2D, Viscous	Small-amplitude waves in multiple superposed viscous fluids

impulse and surface deformation, was obtained by Prosperetti and co-workers in a series of studies (Prosperetti, 1976, 1981; Cortelezzi and Prosperetti, 1981; Prosperetti and Cortelezzi, 1982). It was demonstrated that the time evolution of a standing Fourier mode is governed by a damped harmonic oscillator equation with a memory term. Such memory terms arise in various oscillation problems (Prosperetti, 1980; Berger, 1988) and owe their physical origin to vorticity modes excited due to projections from initial conditions (Prosperetti and Cortelezzi, 1982). In more recent work, the viscous initial-value problem for a pure free-surface deformation (the restoring force being either capillary–gravity or capillarity alone) with zero vorticity initially, has been studied in different base state geometries (Farsoiya et al., 2017, 2020) leading to similar equations with memory terms. Of interest also, is the persistence of this term, when oscillatory forcing is included leading to parametric instabilities. In the viscous case, viscous standing waves under oscillatory forcing have been shown to be governed by damped Mathieu equation with memory term, in various configurations (Beyer and Friedrich, 1995; Cerda and Tirapegui, 1997, 1998; Patankar et al., 2022).

For a stratified fluid, numerous studies have been concerned with the initial value problem of the generation of internal waves from a point or a line source; stationary, moving, or oscillating source, dipoles; moving or oscillating cylinders and spheres; and topography and tidal flows. These are as summarised in Sutherland (2010). For an inviscid, uniformly stratified fluid assumed to be unbounded along all directions (i.e. without a free surface), the initial value problem for a wave number **k** was solved by Lighthill (1996) using the stationary-phase method with arbitrary initial perturbations and a solenoidal distribution of initial velocities. For three-dimensional internal gravity waves, he showed that the amplitude decreases as $t^{-3/2}$ at large times. Wu and Mei (1967) studied the generation of internal and surface waves by an impulsive point source (starting at $t = 0$). Using Fourier (in space) and Laplace (in time) transforms, they found steady-state surface wave solutions for large times and at large distances and the attenuation rate of internal gravity waves. Voisin (1991) studied the internal waves generated by monochromatic and impulsively started point source using a Green's function formulation. Using asymptotic theory, he studied the behaviour of Green's function for the case of a non-Boussinesq point source at small and large times. Later, the same technique was

applied to the case of a pulsating spherical source and to moving point sources (Voisin, 1994). Simakov (1993) subsequently extended the same for various boundary conditions. The Cauchy–Poisson initial value problem in an inviscid, axisymmetric, stratified fluid with a free surface has been studied by Debnath and Guha (1989). For initial free-surface perturbations, they found only the contribution of surface and internal waves at long times and large distances. Similarly, Rollins and Debnath (1992) found the contribution only from the surface and internal-inertial waves with the inclusion of a rotating background. Later, a similar study with a Cartesian 2D domain has been reported by Ghosh et al. (2000) where the author used the stationary phase method to derive an equation for the behaviour of the interface at large times. Although the study considers an infinite depth domain, the implementation of the no-penetration boundary condition ($w = 0$) at $z \rightarrow -\infty$ neglects the presence of a continuous spectrum.

For an unbounded, viscous, stratified liquid, a similarity solution was provided by Thomas and Stevenson (1972) for oscillating localised disturbances using transformation of coordinates. These results have been validated for large distances with particle displacements from experimental measurements. When the fluid is bounded between two flat plates (Gurski et al., 2004) showed, analytically, the existence of a countable infinite set of non-oscillatory normal modes in addition to the internal wave modes. Table 1 summarises representative literature focused on analytical solutions to IVPs (and also normal mode analysis) for stratified and unstratified cases in the linear approximation.

Our aim in the present study is an analytical and simulational investigation of the effect of vortical and free-surface perturbations on the evolution of surface and internal waves on a stratified pool of liquid, taking into account gravity as well as surface tension. By considering effects of stratification, our results extend the classical results due to Lamb (1932) and Yih (1960), Prosperetti (1976) and Prosperetti and Cortelezzi (1982) to vortical perturbations on a viscous, stratified liquid pool. We allow deformation of the free surface and assume that it is not covered by a monolayer (Lucassen-Reynders and Lucassen, 1970). Consequently it is devoid of elastic or viscous properties, eliminating the possibility of "longitudinal" or "transverse" capillary waves (Lucassen, 1968; Felderhof, 2006). The capillary–gravity waves which however do appear in our analysis correspond to the ones appearing at the free surface of a pure viscous liquid, possessing constant surface tension. Such waves are of mixed character and cannot be classified as being purely transverse or longitudinal. The theoretical results presented here significantly extend the earlier results by Cortelezzi and Prosperetti (1981) as well as Prosperetti and Cortelezzi (1982), who presented the linear theory for the effect of vorticity initial conditions on an unstratified, viscous liquid layer with a free surface. The inclusion of viscosity, especially in the unstratified case, is important as this allows the temporal evolution of vorticity eigenmodes, within the linear approximation. Our analytical results may also be viewed as being complementary to those in Rednikov et al. (2000) who studied (via normal mode and a weakly nonlinear analysis), internal and dilatational surface waves due to instabilities arising from a top heated air layer, overlying a liquid layer of finite depth. Incidentally, these authors (Rednikov et al., 2000) did not allow for deformation of the free surface (page 59, section 2 in Rednikov et al. (2000)); thus the capillary waves that they obtain are purely dilatational in contrast to the ones that we report here. The study is organised as follows: in the next section, we present analytical solutions to the IVP for a range of initial conditions on a stratified and unstratified liquid pool. The predictions are rationalised by comparing against the temporal spectrum in all cases. These predictions are then tested against numerical simulations of the Navier–Stokes equations with density stratification, conducted using the open source code Basilisk (Popinet, 2014). We discuss these comparisons and conclude with a summary of salient observations and future scope.
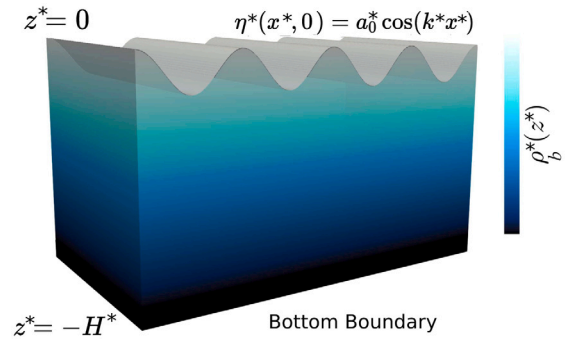

Fig. 2. A schematic of the geometry. In the base state, there is quiescent fluid with a flat free-surface. The base state density profile $\rho_b^*(z^*)$ varies linearly with depth. The schematic is depicted in three dimensions for illustration. The analysis is conducted in two spatial dimensions.

2. Perturbations on a stratified liquid layer: initial value problem

2.1. Governing equations: Boussinesq approximation

As depicted in Fig. 2, consider a pool of depth H^* comprising of quiescent, density-stratified fluid (uniform stratification) bounded at the top with a free surface and at the bottom by a wall. Assuming density to be a (linear) function of temperature T (and independent of other thermodynamic variables like salinity and pressure), we obtain the Boussinesq set of equations (Vallis, 2017; Foster and Saffman, 1970) governing variations in velocity, pressure and density inside the pool viz.

$$\boldsymbol{\nabla}^* \cdot \tilde{\mathbf{u}}^* = 0, \qquad \frac{D\tilde{\mathbf{u}}^*}{Dt^*} = -\frac{1}{\rho_{\text{ref}}}\boldsymbol{\nabla}^*\tilde{p}^* + \frac{\tilde{\rho}^*}{\rho_{\text{ref}}}\mathbf{g} + \frac{\mu}{\rho_{\text{ref}}}\nabla^{*2}\tilde{\mathbf{u}}^* \qquad (1\text{a,b})$$

$$\frac{D\tilde{\rho}^*}{Dt^*} = \kappa \nabla^{*2}\tilde{\rho}^* \qquad (1\text{c})$$

where $\tilde{\mathbf{u}}^* = (\tilde{u}^*, \tilde{w}^*)$, $\mathbf{g} = (0, -g)$, ρ_{ref} is a reference density and κ is the thermal/mass diffusivity. The base state whose stability is being investigated comprises of a quiescent viscous fluid with a density profile $\rho_b^*(z)$ and uniform viscosity μ, with pressure field satisfying the hydrostatic balance $\frac{dp_b^*}{dz^*} = -\rho_b^*(z^*)g$. Note that all base state quantities are indicated with the subscript '*b*' while dimensional quantities have an asterisk. Eqs. (1)a,b and (1)c are supplemented with boundary conditions at the free surface ($z^* = \eta^*$) and the wall ($z^* = -H^*$). These are

$$\frac{D\eta^*}{Dt^*} = \left(\tilde{\mathbf{u}}^* \cdot \mathbf{e}_z\right)_{z^* = \eta^*} \qquad (2\text{a})$$

$$\left(\mathbf{t} \cdot \underline{\underline{\tilde{\sigma}}}^* \cdot \mathbf{n}\right)_{z^* = \eta^*} = 0 \qquad (2\text{b})$$

$$\left(\mathbf{n} \cdot \underline{\underline{\tilde{\sigma}}}^* \cdot \mathbf{n}\right)_{z^* = \eta^*} = -\tau \left(\boldsymbol{\nabla}^* \cdot \mathbf{n}\right)_{z^* = \eta^*} \qquad (2\text{c})$$

$$\tilde{\rho}^*(x^*, z^* = \eta^*, t^*) = \rho_b^*(\eta^*) \qquad (2\text{d})$$

$$\tilde{\mathbf{u}}^*(x^*, z^* = -H^*, t^*) = 0 \qquad (2\text{e})$$

$$\tilde{\rho}^*(x^*, z^* = -H^*, t^*) = \rho_b^*(-H^*) \qquad (2\text{f})$$

where $\mathbf{t}$ and $\mathbf{n}$ are the unit tangent and normal to the perturbed interface, $\underline{\underline{\tilde{\sigma}}}^*$ is the stress tensor and $\mathbf{e}_z$ is a unit normal along the z-direction. Eqs. (2a)–(2f) are the kinematic boundary condition, the zero shear stress condition, the jump in normal stresses due to surface tension τ at the free surface, constant density condition at the interface, the zero-velocity condition at the bottom wall, and constant density condition at the bottom wall respectively. Decomposing all dependent variables as a sum of base and perturbation variables viz.

$$\tilde{\mathbf{u}}^* = \mathbf{0} + \mathbf{u}^*, \quad \tilde{p}^*(\mathbf{x}^*, t^*) = p_b^*(z^*) + p^*(\mathbf{x}^*, t^*), \quad \tilde{\rho}^*(\mathbf{x}^*, t^*) = \rho_b^*(z^*) + \rho^*(\mathbf{x}^*, t^*).$$

Substituting in Eqs. (1)a,b,c and (2a)–(2f), linearising in the perturbed variables (disturbances are small compared to the base state) we obtain in component form

$$\frac{\partial u^*}{\partial x^*} + \frac{\partial w^*}{\partial z^*} = 0 \tag{3a}$$

$$\frac{\partial u^*}{\partial t^*} = -\frac{1}{\rho_{\text{ref}}} \frac{\partial p^*}{\partial x^*} + \frac{\mu}{\rho_{\text{ref}}} \nabla^{*2} u^* \tag{3b}$$

$$\frac{\partial w^*}{\partial t^*} = -\frac{1}{\rho_{\text{ref}}} \frac{\partial p^*}{\partial z^*} - \frac{\rho^*}{\rho_{\text{ref}}} g + \frac{\mu}{\rho_{\text{ref}}} \nabla^{*2} w^* \tag{3c}$$

$$\frac{\partial \rho^*}{\partial t^*} + \left(\frac{d\rho_b^*}{dz^*} \right) w^* = \kappa \nabla^{*2} \rho^* \tag{3d}$$

with the corresponding linearised boundary conditions obtained from using Taylor series expansion about $z^* = 0$,

$$\frac{\partial \eta^*}{\partial t^*} = w^*(x^*, 0, t^*) \tag{4a}$$

$$\frac{\partial u^*}{\partial z^*}(x^*, 0, t^*) + \frac{\partial w^*}{\partial x^*}(x^*, 0, t^*) = 0 \tag{4b}$$

$$\rho_b^*(0) g \eta^* - p^*(x^*, 0, t^*) + 2\mu \frac{\partial w^*}{\partial z^*}(x^*, 0, t^*) - \tau \left(\frac{\partial^2 \eta^*}{(\partial x^*)^2} \right) = 0 \tag{4c}$$

$$\rho^*(x^*, 0, t^*) = 0 \tag{4d}$$

$$u^*(x^*, -H^*, t^*) = w^*(x^*, -H^*, t^*) = \rho^*(x^*, -H^*, t^*) = 0 \tag{4e}$$

where we have used the Newtonian constitutive relation $\underline{\tilde{\sigma}}^* = -\tilde{p}^* \, \underline{\mathbf{I}} + \mu \left[\boldsymbol{\nabla} \tilde{\mathbf{u}}^* + (\boldsymbol{\nabla} \tilde{\mathbf{u}}^*)^\top \right]$. Note that we have used $p_b^*(0) = 0$ in (4c).

2.2. Non-dimensional equations

We now non-dimensionalise Eqs. (3a)–(3d) and boundary conditions (4a)–(4e) using the length, velocity, time, density and pressure scales L, U, L/U, ρ_{ref} and $\rho_{ref} U^2$ respectively to obtain (unstarred variables are non-dimensional)

$$\frac{\partial u}{\partial x} + \frac{\partial w}{\partial z} = 0 \tag{5a}$$

$$\frac{\partial u}{\partial t} = -\frac{\partial p}{\partial x} + \frac{1}{Re} \left(\frac{\partial^2}{\partial x^2} + \frac{\partial^2}{\partial z^2} \right) u \tag{5b}$$

$$\frac{\partial w}{\partial t} = -\frac{\partial p}{\partial z} + \frac{1}{Re} \left(\frac{\partial^2}{\partial x^2} + \frac{\partial^2}{\partial z^2} \right) w - \left(\frac{gL}{U^2} \right) \rho \tag{5c}$$

$$\frac{\partial \rho}{\partial t} + \left(\frac{d\rho_b}{dz} \right) w = \frac{1}{RePr} \left(\frac{\partial^2}{\partial x^2} + \frac{\partial^2}{\partial z^2} \right) \rho \tag{5d}$$

and the boundary conditions

$$\frac{\partial \eta}{\partial t} = w(x, 0, t) \tag{6a}$$

$$\frac{\partial u}{\partial z}(x, 0, t) + \frac{\partial w}{\partial x}(x, 0, t) = 0 \tag{6b}$$

$$\rho_b(0)\eta - \left(\frac{U^2}{gL} \right) p(x, 0, t) + \frac{2}{Re} \left(\frac{U^2}{gL} \right) \frac{\partial w}{\partial z}(x, 0, t) - \frac{1}{Bo} \left(\frac{\partial^2 \eta}{\partial x^2} \right) = 0 \tag{6c}$$

$$\rho(x, 0, t) = 0 \tag{6d}$$

$$u(x, -H, t) = w(x, -H, t) = \rho(x, -H, t) = 0 \tag{6e}$$

The non-dimensional numbers are the Reynolds number $Re \equiv \frac{\rho_{\text{ref}} L U}{\mu}$, the Bond number $Bo \equiv \frac{\rho_{\text{ref}} g L^2}{\tau}$, the Richardson number $Ri \equiv \frac{-\frac{g}{\rho_{\text{ref}}} \left(\frac{d\rho_b^*}{dz^*} \right) L^2}{U^2}$, the Prandtl number $Pr \equiv \frac{\mu}{\rho_{\text{ref}} \kappa}$ and the ratio $H \equiv H^*/L$. We choose the length and the velocity scale L and U to be $1/k$ and $\sqrt{g/k}$ respectively viz. the length-scale and phase speed of a surface gravity wave. Therefore, the ratio $\frac{gL}{U^2}$ (can be defined as inverse Froude number squared) which appears in Eq. (6c) turns out to be unity. Also, the Richardson number Ri here becomes N^2/ω^2, i.e. buoyancy frequency non-dimensionalised with deep-water surface wave frequency.

All equations and boundary conditions are Fourier and Laplace transformed in x and t respectively. As k is used in non-dimensionalising lengths, the Fourier–Laplace transformed variables (indicated with an overbar) are thus independent of k. Eliminating pressure $\bar{p}(z, s)$ through cross differentiation and defining the perturbation stream-function $\bar{\psi}(z, s)$, we obtain after some algebra the following equation.

$$\left[(D^2 - 1) - sRePr \right] \left[\left((D^2 - 1) - sRe \right) (D^2 - 1) \bar{\psi}(z, s) - Ri \, Re^2 Pr \bar{\psi}(z, s) \right]$$
$$= \mathbf{i} Re^2 Pr \hat{\rho}(z, t = 0) + Re \left[(D^2 - 1) - sRePr \right] \hat{\omega}(z, t = 0) \tag{7}$$

where $D \equiv \partial/\partial z$, is the differentiation operator and where $\mathbf{i} \equiv \sqrt{-1}$. Eq. (7) is the initial–boundary-value problem that we need to solve in order to determine the evolution of the perturbation streamfunction $\bar{\psi}(s, z)$. This is supplemented by boundary conditions which in the Fourier–Laplace domain are:

$$(D^2 + 1)\bar{\psi}(s, z = 0) = 0 \tag{8a}$$

$$s\left((D^2 - 3) - sRe \right) D\bar{\psi}(s, z = 0) - Re(1 + Bo^{-1})\bar{\psi}(s, z = 0)$$
$$= Re(1 + Bo^{-1})\mathbf{i}\hat{\eta}(t = 0) - sReD\hat{\psi}(t = 0, z = 0) \tag{8b}$$

$$\left[s - \frac{1}{Re}(D^2 - 1) \right](D^2 - 1)\bar{\psi}(s, z = 0) = -\hat{\omega}(z = 0, t = 0) \tag{8c}$$

$$\bar{\psi}(s, -H) = 0, \quad D\bar{\psi}(s, -H) = 0,$$

$$\left[s - \frac{1}{Re}(D^2 - 1) \right](D^2 - 1)\bar{\psi}(s, -H) = -\hat{\omega}(z = -H, t = 0) \tag{8d,e,f}$$

We remind the reader that Eq. (8a) represents the zero shear stress condition at the linearised free-surface $z = 0$. Eq. (8b) is the normal stress boundary condition at $z = 0$, also taking into account the kinematic boundary condition. Eqs. (8c) and (8f) enforce the vanishing of density perturbations at the free surface and the bottom-wall (when depth is finite) respectively. Eqs. (8d) and (8e) are the no-penetration and no-slip conditions at the wall. The stratified and the unstratified ($Ri = 0, Pr \to \infty$ and $\hat{\rho} = 0$) limits differ in the order of the equation governing $\bar{\psi}(s, z)$. In the former case, Eq. (7) is sixth order (see eqn. 104 in chapter II in Chandrasekhar (1981) for a similar sixth order equation) while for the latter, it is a fourth order equation. Consequently, the boundary conditions for solving Eq. (7) are chosen accordingly e.g. for the infinite-depth, stratified layer, we choose to impose conditions (8a), (8b) and (8c) at $z = 0$ along with $\bar{\psi} \to$ finite as $z \to -\infty$. On the other hand, for the unstratified, finite depth layer, we implement boundary conditions (8a) and (8b) at $z = 0$ and Eqs. (8d) and (8e) at $z = -H$ and so on.

In solving Eq. (7) for the stratified case, the homogeneous part to the solution maybe chosen to be of the form $\sim C_i e^{\lambda_i z}$ and using the method of variation of parameters, we can write the general solution as

$$\bar{\psi}(s, z) = \sum_{i=1}^{6} \exp(\lambda_i z) \left[C_i(s) + \int^z \frac{Adj(\mathscr{W})_{i,6}(s, z')\mathscr{R}(s, z')}{|\mathscr{W}(s, z')|} dz' \right] \tag{9}$$

Here, $\mathscr{R}(s, z)$ is the RHS of Eq. (7), $|\mathscr{W}(s, z)|$ is the sixth-order Wronskian (supplementary material) constructed from the homogeneous part to the solution while Adj($\mathscr{W}$) represents the adjugate of the Wronskian matrix, the subscripts indicating the elements of this matrix. It is shown in the supplementary material that expression (9) maybe rewritten as (Riley et al. (2006), page 510):

$$\bar{\psi}(s, z) = \sum_{i=1}^{6} \exp(\lambda_i z) \left[C_i(s) + \mathscr{E}_i(s) I_i(s, z) \right], \text{ with}$$

$$\mathscr{E}_i(s) \equiv \frac{1}{\prod_{j=1, j \neq i}^{6} (\lambda_i - \lambda_j)}, \quad I_i(s, z) \equiv \int \exp(-\lambda_i z)\mathscr{R}(s, z) dz. \tag{10}$$

In the following sub-section(s), we determine expressions for $C_i(s)$ subject to various initial conditions for specific limits like a stratified or an unstratified layer, of finite or infinite depth. These are then employed to obtain explicit expression(s) for the perturbation $\hat{\psi}(z, t)$ post Laplace inversion.

2.3. Linearised analytical predictions

First consider the case when the liquid layer is stratified and of finite depth. By substituting Eq. (10) in the boundary conditions given by Eqs. (8a)–(8d,e,f), we can obtain a linear set of equations for $C_i(s)$ ($i = 1, 2 \ldots 6$). These maybe expressed symbolically as,

$$\sum_{i=1}^{6} \mathscr{D}_{ji}(s) C_i(s) = \mathscr{R}_j(s), \quad j = 1, 2 \ldots 6 \tag{11}$$

where, $\mathscr{D}_{ji}(s)$ is the coefficient matrix (i.e. the matrix which yields the dispersion relation if one were to do normal mode analysis). $C_i(s)$ are the coefficients in Eq. (10) and $\mathscr{R}_j(s)$ is a column matrix of remaining terms in the boundary conditions (8a)–(8d,e,f), taken to the right hand side. Eqs. (11) may be solved for the $C_i(s)$ to obtain,

$$C_i(s) = \frac{1}{|\mathscr{D}(s)|} \sum_{j=1}^{6} Adj(\mathscr{D}(s))_{ij} \mathscr{R}_j(s). \tag{12}$$

Substituting expression (12) into (10) and transferring from the Laplace to time domain, we obtain formally

$$\hat{\psi}(t, z) = \frac{1}{2\pi i} \int_{\gamma - i\infty}^{\gamma + i\infty} \exp(st) ds \sum_{i=1}^{6} \exp(\lambda_i(s) z)$$

$$\times \left[\sum_{j=1}^{6} \frac{1}{|\mathscr{D}(s)|} Adj(\mathscr{D}(s))_{ij} \mathscr{R}_j(s) + \mathscr{E}_i(s) I_i(s, z) \right]. \tag{13}$$

Here onwards, we obtain explicit expressions for the perturbation stream-function $\hat{\psi}(z, t)$ using Eq. (13) by choosing explicit initial conditions and using Cauchy residue theorem to evaluate the corresponding Bromwich contour integral. One can similarly obtain corresponding expressions for the free-surface perturbation $\hat{\eta}(t)$ and the density perturbation $\hat{\rho}(z, t)$. In order to see that Eq. (13) depends explicitly on initial conditions, note that it has $I_i(s, z)$ on the right hand side which in turn depends on $\mathscr{R}(s, z)$ see expression (10), the latter explicitly depending on the initial density and vorticity perturbation viz. $\hat{\rho}(z, t = 0)$ and $\hat{\omega}(z, t = 0)$ respectively, from RHS of Eq. (7). In addition, $\mathscr{R}_j(s)$ in Eq. (13) also contains the free surface initial condition. In the following sub-section, we choose these initial conditions corresponding to vorticity and free-surface perturbations for which (13) yields exact solutions. The next two sub-sections present these analytical solutions in the context of a stratified layer and an unstratified layer respectively while comparing these to the discrete temporal spectrum of the problem.

2.3.1. Stratified layer (Ri $\neq$ 0) of finite depth

The algebra for specific initial conditions is lengthy but straightforward and the reader is referred to the accompanying supplementary material where exact expressions are derived. We focus on the specific case of vortical initial perturbation on a stratified pool of finite depth here. Assuming an initial localised, vorticity perturbation of the form $\hat{\omega}(z, t = 0) = \Omega \exp\left(-\frac{(z - z_d)^2}{d^2}\right)$, where $z_d \in (-H, 0)$ and no initial density ($\hat{\rho}(z, t = 0) = 0$) or free-surface perturbations ($\hat{\eta}(t = 0) = 0$), we wish to obtain the expression of $\hat{\psi}(t, z)$ for this initial condition from Eq. (13). Eq. (13) may be converted into a contour integral on the complex s plane and the integral evaluated using Cauchy residue theorem. The final expression is then written as the summation of the residues at all the zeros of the dispersion matrix ($|\mathscr{D}(s)|$) as,

$$\hat{\psi}(z, t) = \sum_{n=1}^{\infty} \frac{1}{|\mathscr{D}(s_n)|'} \exp(s_n t) \sum_{i=1}^{6} \exp(\lambda_i(s_n) z) \left[\sum_{j=1}^{6} Adj(\mathscr{D}(s_n))_{ij} \mathscr{R}_j(s_n) \right]. \tag{14}$$

It should be noted that no poles are found for the second term on the right hand side of expression (13) and thus this term does not appear in Eq. (14). Similarly the expression for the perturbed free-surface is

$$\frac{\hat{\eta}(t)}{\hat{\eta}(0)} = 1 - \frac{i}{\hat{\eta}(0)} \sum_{n=1}^{\infty} \exp(s_n t) \sum_{i=1}^{6} \left[\frac{1}{s_n |\mathscr{D}(s_n)|'} \sum_{j=1}^{6} Adj(\mathscr{D}(s_n))_{ij} \mathscr{R}_j(s_n) \right]$$

$$- \frac{i}{\hat{\eta}(0)} \sum_{i=1}^{6} \left[\frac{1}{|\mathscr{D}(0)|} \sum_{j=1}^{6} Adj(\mathscr{D}(0))_{ij} \mathscr{R}_j(0) \right]. \tag{15}$$

A similar equation for the density evolution can also be obtained, although this is not provided here (see supplementary material). For understanding the temporal evolutions predicted in Eqs. (14) and (15) qualitatively, it is useful to plot the temporal eigenvalue spectrum for this case. Plotted in Fig. 3, panel (a) are the roots of $\mathscr{D}(s)$ (Eq. (12)) calculated numerically in Mathematica (Inc., 2022) on the complex s plane (note that the vertical axis is real while the horizontal is imaginary). The physical parameters for this plot are chosen corresponding to case (c) in Table 2. As seen, there are two underdamped surface gravity (SG) modes (deep-blue circles) arising from viscous corrections to the inviscid, irrotational capillary–gravity waves with dispersion relation $\omega^2 = \left(gk + \frac{\tau k^3}{\rho}\right) \tanh(kH)$. These may be identified by the exponentially decaying vertical structure of their eigen-functions. Note that despite the inclusion of surface tension, we refer to the surface modes as SG (surface-gravity) modes rather than capillary–gravity modes. In addition, in Fig. 3a there is a countably infinite set of purely damped modes (sky blue circles, also see inset) which we term vorticity modes as they do not owe their origin to the presence of the free surface. Also shown in this figure are the internal gravity (IG) modes (red circles). These modes may be identified by their non-zero phase speed and a vertical structure that spans the domain. The infinite summations in Eqs. (14) and (15) reflect the contributions from these discrete modes shown in Fig. 3, panel a. For reference, panel (b) in the same figure provides the spectrum for the inviscid case. Here we observe the absence of the vorticity modes, while the IG modes become countably infinite in agreement with the inviscid predictions of Yih (1960). In other words, viscosity eliminates IG modes of shorter wavelengths making the set of IG modes finite.

### 2.3.2. Stratified, deep water limit: H $\rightarrow$ ∞

Here we examine the deep water limit of a stratified, pool of viscous liquid. In this limit the governing Eq. (7) remains unchanged while the free surface boundary conditions in Eqs. (8a), (8b) and (8c) also remain valid in this limit. However boundary conditions (8d,e,f) need to be replaced by suitable finiteness conditions as $z \rightarrow -\infty$. It is shown in the supplementary material in this limit $H \rightarrow \infty$, the perturbation stream-function may be written in the same form as Eq. (14), although now the $C_i(s)$ have different expressions compared to the finite depth case in Eq. (12). It is of interest to ask, what are the features of the infinite-depth counterpart of the spectrum in Fig. 4(b). We note that this was studied earlier by Yih (1960), demonstrating that in the inviscid, stratified, infinite depth limit, if there is no density discontinuity in the domain, there is no discrete spectrum and only a continuous one (see discussion in Yih (1960), page 496 second paragraph.)

2.3.3. Unstratified layer (Ri = 0) of finite depth

Having discussed the spectrum for the stratified case, we now turn to the unstratified limit where the Richardson number is Ri = 0. We recall that for the unstratified case, Eq. (7) is a fourth order equation. Analogous to the earlier section, the expression for the perturbation stream-function after Laplace inversion viz. $\hat{\psi}(z, t)$ is obtained as (note the sum over four roots rather than six in the unstratified case here)

$$\hat{\psi}(z, t) = \frac{1}{2\pi i} \int_{\gamma - i\infty}^{\gamma + i\infty} \exp(st) ds \sum_{i=1}^{4} \exp(\lambda_i(s) z)$$

$$\times \left[\sum_{j=1}^{4} \frac{1}{|\mathscr{D}(s)|} Adj(\mathscr{D}(s))_{ij} \mathscr{R}_j(s) + \mathscr{F}_i(s) I_i(s, z) \right]. \tag{16}$$

Like earlier, for a localised vortical initial condition (with no free-surface perturbation) $\hat{\omega}(z, t = 0) = \Omega \exp(-(z - z_d)^2/d^2)$, where $z_d \in (-H, 0)$, we use Cauchy residue theorem to evaluate the Bromwich

(a) Viscous spectrum   (b) Inviscid spectrum
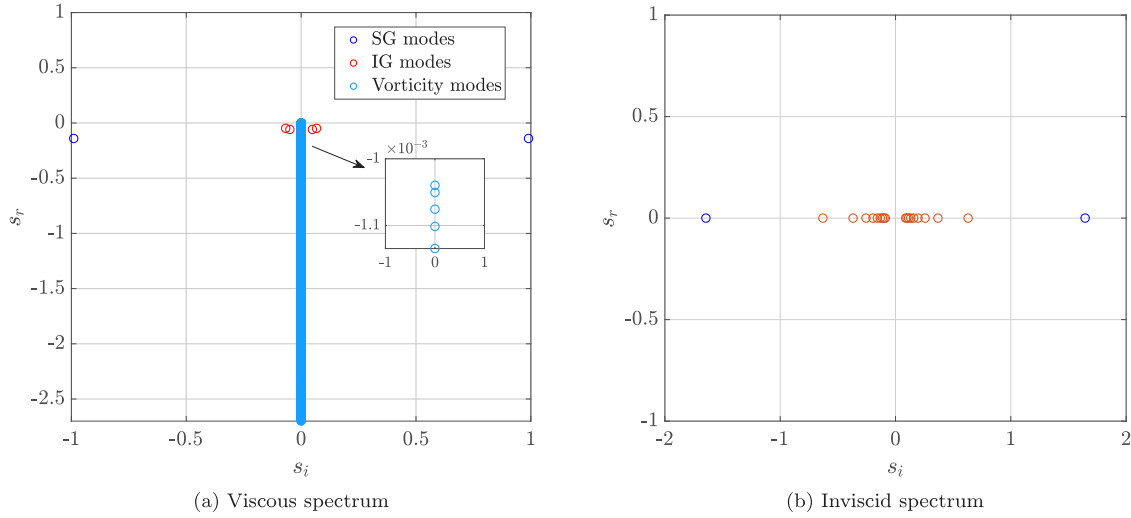
Fig. 3. Temporal eigenvalue spectrum for a stratified, pool of finite depth: Panel (a) The viscous discrete spectrum modes obtained by numerically solving the determinant eqn. $\mathscr{D}(s) = 0$ (see eq. (12)). Note that the imaginary axis s_i has been plotted horizontally instead of vertically. Deep blue circles correspond to under-damped surface gravity (SG) modes. Circles in red represent damped internal gravity (IG) modes. Circles in sky-blue (also in the inset) correspond to damped vorticity modes. We plot the corresponding inviscid spectrum in panel (b). In the inviscid limit, all the vorticity modes of panel (a) (sky blue circles) collapse to the origin in panel (b). In this limit, the IG modes are countably infinite (Yih, 1960), only some of which are depicted in panel (b). In the viscous case in panel (a) we could numerically find only four IG modes. The parameters for the plots correspond to case c in Table 2. (For interpretation of the references to colour in this figure legend, the reader is referred to the web version of this article.)

contour integral for Eq. (16) to obtain the perturbation stream-function. This is

$$\hat{\psi}(z,t) = \sum_{n=1}^{\infty} \sum_{i=1}^{4} \exp(\lambda_i(s_n)z) \left[\frac{1}{|\mathscr{D}(s_n)|'} \sum_{j=1}^{4} Adj(\mathscr{D}(s_n))_{ij} \mathscr{R}_j(s_n) \right] \exp(s_n t).$$

(17)

On the other hand, for a free-surface initial perturbation $\hat{\eta}(0)$ and zero vorticity initial condition, the free-surface at a later time t is predicted to be

$$\frac{\hat{\eta}(t)}{\hat{\eta}(0)} = 1 - \frac{\mathbf{i}}{\hat{\eta}(0)} \sum_{n=1}^{\infty} \sum_{i=1}^{4} \left[\frac{1}{s|\mathscr{D}(s_n)|'} Adj(\mathscr{D}(s_n))_{ij} \mathscr{R}_j(s_n) \right] \exp(s_n t)$$

$$- \frac{\mathbf{i}}{\hat{\eta}(0)} \sum_{i=1}^{4} \left[\frac{1}{|\mathscr{D}(0)|} Adj(\mathscr{D}(0))_{ij} \mathscr{R}_j(0) \right]$$

(18)

Here n runs over all the (simple) roots of $\mathscr{D}(s)$ and a prime indicates differentiation. In order to understand these analytical predictions, it is once again useful to visualise the temporal spectrum from the dispersion relation $\mathscr{D}(s) = 0$ on the complex s plane. This is shown for the present case (unstratified, pool of finite depth) in Fig. 4(a). The two deep blue circles represent the surface-gravity modes which like earlier, are shifted slightly off the imaginary axis due to viscous damping. The light-blue circles once again represent the purely damped, vorticity modes. The inviscid limit of this spectrum is depicted in Fig. 4(b) where there are only two deep blue circles while the vorticity modes collapse to the origin as discussed below.

In order to understand the vorticity modes slightly better, we note that in the absence of background flow and in the unstratified, linearised limit, the transport of perturbation vorticity occurs purely diffusively. This is seen from the diffusion equation governing the equation of perturbation vorticity: $\frac{\partial}{\partial t}(\nabla \times \hat{\boldsymbol{u}}) = -\nu \nabla^2 (\nabla \times \hat{\boldsymbol{u}})$. As indicated by the viscous spectrum in Fig. 4(a), there are a countably infinite set of purely damped, vorticity modes which play an important role in this diffusive process. When we however take the inviscid ($\nu \to 0$) limit, the perturbation vorticity equation becomes trivial predicting $\frac{\partial}{\partial t}(\nabla \times \hat{\boldsymbol{u}}) = 0$. This implies that these vorticity modes (sky blue circles) in Fig. 4(a), all have zero frequency in the inviscid limit explaining their disappearance in Fig. 4(b). The physical implication is that any initial distribution of perturbation vorticity stays frozen in time in

the inviscid limit and can evolve only when viscosity is included in the model. It is known from prior studies (Farsoiya et al., 2017), that for zero vorticity initial condition accompanied by a free-surface deformation i.e. $\hat{\eta}(t = 0)$ and for small value of liquid viscosity, the contribution from these vorticity modes is numerically quite small. In contrast, our choice of a localised vorticity initial perturbation here viz. $\hat{\omega}(z, t = 0) = \Omega \exp\left(-\frac{(z - z_d)^2}{d^2}\right)$ will be made in such a way that this perturbation will have a relatively large projection on the vorticity modes of Fig. 4(a). This prediction will be numerically tested in the next section where in addition, the cases of free-surface initial perturbations will also be considered.

2.3.4. Unstratified, deep water limit: $H \to \infty$

Analogous to the earlier section, the unstratified, viscous, deep water limit is also interesting. Here prior studies have identified the presence of a viscous continuous spectrum (Lamb, 1932; Prosperetti, 1976) in addition to the discrete one. Notably, this continuous spectrum comprises the vorticity modes which were also present in the finite depth case, but constituted a discrete spectrum there. For the case of free-surface perturbations only (zero initial vorticity perturbation), it was shown by Prosperetti (1976) (see eqn. 33 in Prosperetti (1976) with $u_0 = 0$) that the presence of the continuous spectrum may be understood through the multi-valuedness of the dispersion relation. Here in dimensional (Laplace) variables, the point $s = -\nu k^2$ turns out to be branch-point of the viscous, infinite depth dispersion relation necessitating a branch-cut in the Laplace domain, necessary for contour integration. It was already remarked upon by Lamb (1932) (see the discussion around eqn. 26 in Lamb (1932), section 349) that in the infinite depth limit, the continuous spectrum (CS) modes do not decay with depth but instead possess a sinusoidal, oscillatory character persisting up to $z \to -\infty$. A general vortical initial condition may have large projection on these continuous spectrum modes depending on the depth where the initial vorticity distribution is concentrated. We will return to this point when we compare our simulations with analytical predictions in the next section.

3. Numerical simulations

In this section, we briefly describe the numerical simulations of a density-stratified, viscous liquid layer with a free-surface. As discussed
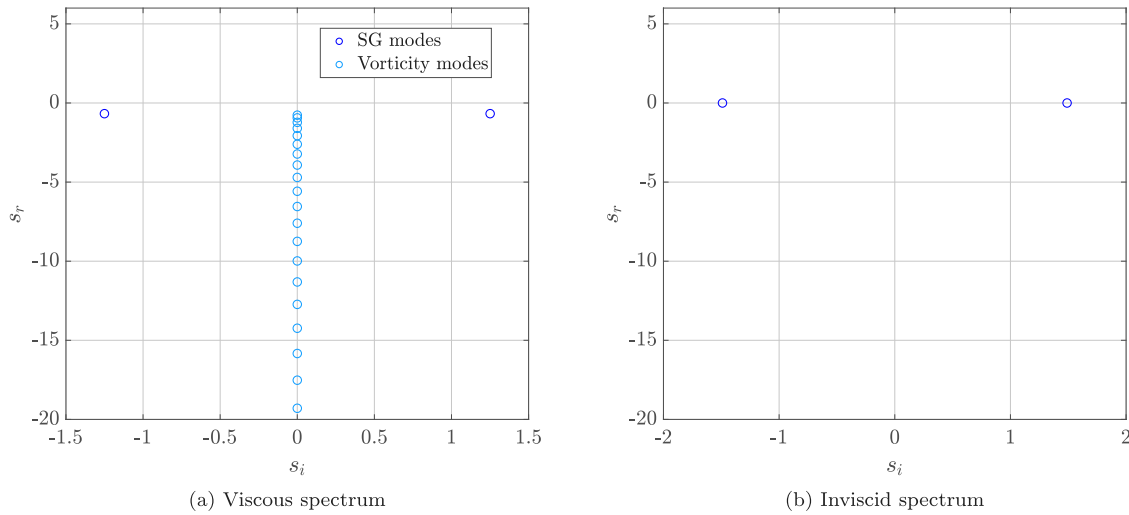
Fig. 4. The discrete spectrum modes obtained by numerically solving $D(s) = 0$ for an unstratified layer corresponding to Case (a) in Table 2. The symbols indicate roots of $\mathscr{D}(s)$ in the complex Laplace domain s. (a) The two modes indicated as deep blue circles corresponded to under-damped capillary–gravity modes while those in sky-blue correspond to purely damped, vorticity modes. (b) In the inviscid limit, the deep-blue circles correspond to two roots from the capillary–gravity dispersion relation $\omega^2 = \left(gk + \frac{\tau k^3}{\rho}\right)\tanh(kH)$. (For interpretation of the references to colour in this figure legend, the reader is referred to the web version of this article.)

earlier, we impose small amplitude, initial vortical and free surface perturbations, tracking their spatio-temporal evolution. The simulations are carried out using the open-source code Basilisk (Popinet, 2014). This code numerically solves the Navier–Stokes equations and has been benchmarked quite extensively against a wide range of interfacial flow problems e.g. Farsoiya et al. (2023), Sanjay et al. (2022), Kayal et al. (2022), Singh et al. (2019) and Basak et al. (2021). Basilisk is used to solve the following equations

$$\boldsymbol{\nabla} \cdot \mathbf{u} = 0, \quad \frac{\partial \mathbf{u}}{\partial t} + \boldsymbol{\nabla} \cdot (\mathbf{u} \otimes \mathbf{u}) = -\frac{1}{\rho_{\text{ref}}} \boldsymbol{\nabla} p + \frac{\mu}{\rho_{\text{ref}}} \nabla^2 \mathbf{u} + \mathbf{F}_b + \frac{T}{\rho_{\text{ref}}} \kappa \delta_s \mathbf{n} \quad (19)$$

$$\frac{\partial f}{\partial t} + \boldsymbol{\nabla} \cdot (f\mathbf{u}) = 0 \quad (20)$$

In Eqs. (19) and (20), $\mathbf{u}$, p and f are the velocity, pressure and volume fraction fields respectively and $\mathbf{F}_b$ represents a body force related to buoyancy (see below). T is the coefficient of surface tension, κ is the curvature associated with a particular point at the interface with $\mathbf{n}$ as the unit normal vector at that point, while ρ_{ref} and μ denote the reference density and dynamic viscosity of the fluid in the computational domain given by the expressions

$$\rho_{\text{ref}} = f\rho_{\text{ref}}^{(\mathcal{L})} + (1-f)\rho^{(\mathcal{G})} \quad (21)$$

$$\mu = f\mu^{(\mathcal{L})} + (1-f)\mu^{(\mathcal{G})} \quad (22)$$

where the superscripts $\mathcal{L}$ and $\mathcal{G}$ refer to values in the liquid and gas phases respectively. f is unity in the liquid and zero in the gas phase and cells with $0 < f < 1$ contain the interface (approximated as a free-surface in the theory). In order to incorporate density stratification in the liquid, a body force term $\mathbf{F}_b$ is included in the momentum equation (19) incorporating the Boussinesq approximation viz.

$$\mathbf{F}_b = b\hat{\mathbf{e}}_z = \left[f\left(-\frac{\rho}{\rho_{\text{ref}}}\right)g + (1-f)(-g) \right]\hat{\mathbf{e}}_z. \quad (23)$$

The density field ρ is updated at each time step by numerically solving a tracer diffusion equation following (Antoon van Hooft, 2018),

$$\frac{\partial \rho}{\partial t} + \boldsymbol{\nabla} \cdot (\rho\mathbf{u}) = \nu_T \nabla^2 \rho \quad (24)$$

where ν_T is the thermal diffusivity of the fluid. As the code utilises the one fluid formulation of the VoF algorithm, it solves for both the gas and liquid phases necessarily. We however ignore the gas phase in our analytical calculations. In order to facilitate comparison with theory, we maintain high density ratio value between the liquid phase and the gas phase (i.e. $\rho_{\text{ref}}^{(\mathcal{L})}/\rho^{(\mathcal{G})} = 1000$) in the numerical simulations. The

boundary conditions imposed on the field variables at the four walls of the domain box are elucidated in the Table 3. Using the Poisson equation relating streamfunction and vorticity, the velocity at $t = 0$ is found from the initial vorticity perturbation (as given in Table 2). This velocity is provided as an initial condition in the simulations. The initial free surface perturbation is incorporated by defining the free surface at time $t = 0$ as a sinusoid of amplitude a_0 and wavenumber k. The simulation domain is a square box of size $H*$, i.e., two-wavelengths in horizontal and vertical directions.

4. Results and comparison with theory

In this section, we compare the analytical results from Section 2 with the results from direct numerical simulations (DNS). In the first subsection, we present the results of an unstratified liquid layer perturbed at the interface, without and with initial vorticity (cases a and b in Table 1 respectively). In the next subsection, we discuss simulations of a stratified liquid layer (without interface perturbation) with initial perturbation vorticity at two different values of the Brunt-Vaisala frequency (refer cases c and d in Table 1 respectively). Table 2 describes the boundary conditions used for different parameters in DNS calculations. The thermodynamic and simulation parameters in Table 2 have been chosen to correspond to high density ratio like that of air–water. This is important for the dynamic effect of air to be negligible in the simulations, allowing us to compare with analytical predictions for a stress-free interface (free-surface). However, the dynamic viscosity of the liquid has been deliberately chosen to be significantly higher than water (i.e. we choose $\mu^{\mathcal{L}} = 2$ dyn-s/cm^2 compared to 10^{-3} in same units for water). This is partly motivated by our observations in Farsoiya et al. (2017) that increasing the viscosity of the liquid, increases the numerical contribution from the vorticity modes. The wavelength $\lambda = \frac{2\pi}{k}$ has been chosen small, 1 cm and 5 cms respectively for cases (a), (b) and (c), (d) respectively while the surface tension is chosen to be smaller than that for air–water. Gravity is set to $g = 981$ cm/s^2 for all simulations. For our choice of parameters, the capillary length scale is ≈ 1.7 mm.

Discussion

Figs. 5(a) and 5(b) represent the time evolution of the free-surface perturbation (normalised by its peak initial value) for case (a) and (b) in Table 2. Both simulations represent an unstratified pool with

Table 2
Simulation parameters (in C.G.S. units).

Case	Grid	H^*	k	N	τ	$\mu^{(\mathcal{L})}$	$\mu^{(\mathcal{G})}$	$\rho_{ref}^{(\mathcal{L})}$	$\rho^{(\mathcal{G})}$	ν_T	Ri	Re	Pr	Bo	a_0	Ω	z_d	d	Initial perturbation(s)
(a)	1024×1024	2	2π	–	30	2	0.000185	1	0.001	–	–	0.9943	–	0.8283	0.0079	0	–	–	Free surface only
(b)	1024×1024	2	2π	–	30	2	0.000185	1	0.001	–	–	0.9943	–	0.8283	0.0079	0.05	−1.3	0.1	Free-surface and Vorticity
(c)	1024×1024	10	$\frac{2\pi}{5}$	3	30	2	0.000185	1	0.001	0.001	0.0073	11.1171	2000	20.7075	0	0.0079	−5	1	Vorticity only
(d)	1024×1024	10	$\frac{2\pi}{5}$	10	30	2	0.000185	1	0.001	0.001	0.0811	11.1171	2000	20.7075	0	0.0079	−5	1	Vorticity only
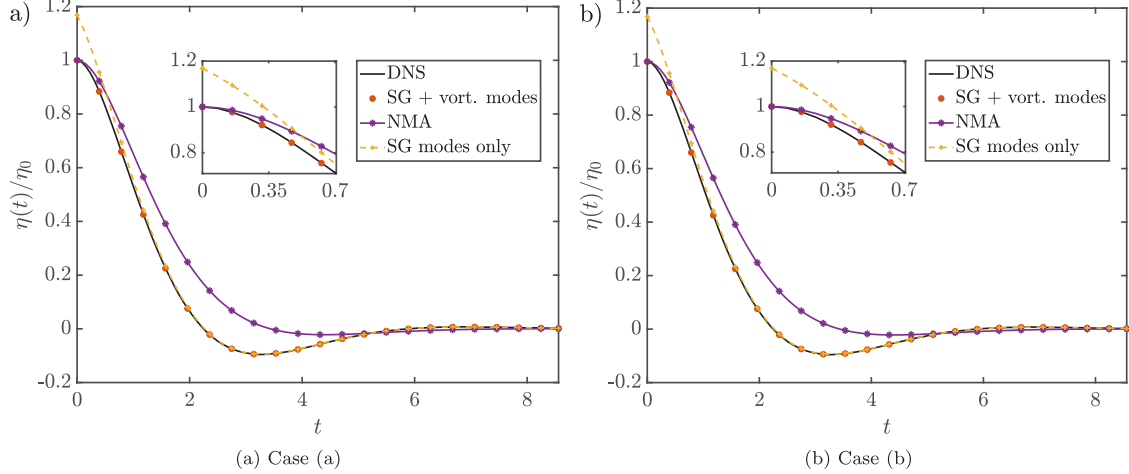
Fig. 5. Free-surface amplitude variation as a function of time for the cases (a) and (b), respectively. The inset is a zoomed in version of the plot at the initial time. The horizontal axis is the non-dimensional time ($t^* \sqrt{g^* k^*}$) and the vertical axis is the non-dimensional amplitude. (For interpretation of the references to colour in this figure legend, the reader is referred to the web version of this article.)

Table 3
Boundary conditions in DNS.

Wall	u		p	f	b
	u_x	u_z			
Top	N	D	N	N	$-g$
Bottom	D	D	N	N	$-g - N^2 H$
Left	D	N	N	N	N
Right	D	N	N	N	N
D: Dirichlet			N: Neumann		

the free surface deformed as a Fourier mode of wavenumber $k = 2\pi$ (i.e. wavelength 1 cm). The two cases however differ in the absence (case a) or presence (case b) of initial perturbation vorticity in the bulk of the pool. The most notable aspect of both figures is that they look indistinguishable despite having different initial conditions in terms of vorticity. We will discuss this important point later on in this section.

The curves in yellow ('SG modes only') in both Figs. 5(a) and 5(b) represent the contribution to the free-surface evolution from the two SG modes only (i.e. the deep blue circles depicted in Fig. 4(a)). A common observation in both figures is that this approximation ('SG modes only') is unable to satisfy the initial conditions at the free-surface viz. $a(0) = a_0$ and $\dot{a}(0) = 0$, see the mismatch between these and the DNS signal at $t = 0$. This is understood as follows: the contribution to the free-surface displacement comes not only from the two SG modes which, by definition, are 'surface modes' but also from the vorticity modes. Independent of whether we impose zero vorticity initial condition in case (a) or an initial, localised vortical perturbation in case (b), these vorticity modes are excited in both cases. Consequently, the contribution of these vorticity modes are necessary (in addition to the contribution from SG modes) for satisfying the conditions $a(0) = a_0$ and $\dot{a}(0) = 0$. This is seen clearly in Figs. 5(a) and 5(b), where the curve labelled as 'SG + vort. modes' (i.e. considering both contributions) satisfies both initial conditions and displays excellent agreement with the DNS signal. At slightly large time, however, the contribution from the vorticity modes

becomes insignificant and the surface response from SG modes only, becomes identical to the DNS response.

Just as the vorticity modes can contribute to the free-surface displacement, the two SG modes in Fig. 4(a) have vorticity associated with them. This vorticity field decays exponentially along the depth of the pool (negative z-direction). An estimate of the depth of penetration of this vorticity field is given by the real part of $\left(k^2 + \tilde{s}/\nu^{(\mathcal{L})}\right)^{-1/2}$ (considering dimensional variables, $s = \frac{\tilde{s}}{\sqrt{gk}}$), which for the parameters corresponding to case (a) and (b) of Table 2 is approximately 0.10 cm. Note that in evaluating this, we have chosen the value of s to be one of the two complex conjugate pairs (SG modes) in Fig. 4(a). It is apparent that this vorticity penetration depth is substantially less than the wavelength of the Fourier mode at the free-surface, which is 1 cm for this case. It is thus intuitively clear that a linear superposition of the two SG modes only, can neither produce a zero initial vorticity field (case (a)) nor satisfy the free-surface initial conditions as already discussed. This is verified in Fig. 6(a) where the vorticity profile at $x = 3.2$ is plotted at $t = 0.079$ as a function of the depth coordinate z. One observes that the curve labelled as 'vort. modes only' in this figure is a poor descriptor of the DNS vorticity profile (black curve). Incidentally, the inability of the vorticity modes only (or alternatively the SG modes only) to satisfy the initial conditions is consistent with our earlier results in Farsoiya et al. (2020) where azimuthal perturbations on a hollow cylindrical filament were studied and similar conclusions, for zero vorticity initial conditions, were reported.

For case (b) in Table 2 the chosen Gaussian shaped, initial vorticity perturbation is centred at $z_d = 1.3$ cm and has a thickness of 0.1 cm. At this depth ($z_d = 1.3$ cm), the vorticity of the SG modes is practically zero (see grey curve in Fig. 6(b)) and the contribution from the countably infinite vorticity modes of Fig. 4(a), becomes crucial in order to express this initial vortical patch. This is verified in Fig. 6(b) where we note the small 'hump' in vorticity in the DNS signal at $z \approx -8$ arising from the initial perturbation. It is seen that the vorticity from the SG modes is zero at this depth, whereas the contribution from the vorticity modes are not. Interestingly, although the curve labelled as 'vorticity modes only' in this figure provides an excellent approximation to the
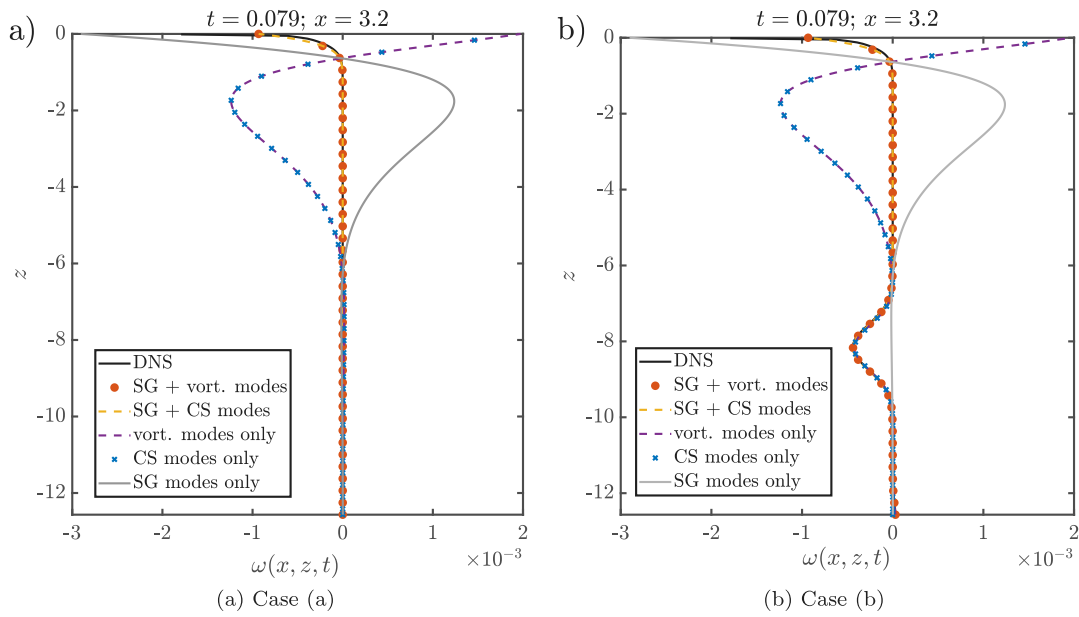
Fig. 6. Vorticity plotted as a function of the vertical coordinate at a particular time $t(= 0.079)$ and horizontal coordinate $x(= 3.2)$ for the cases (a) and (b), respectively. The horizontal axis is the non-dimensional vorticity ($\omega^*/\sqrt{g^* k^*}$) and the vertical axis is the non-dimensional vertical coordinate ($z^* k^*$).
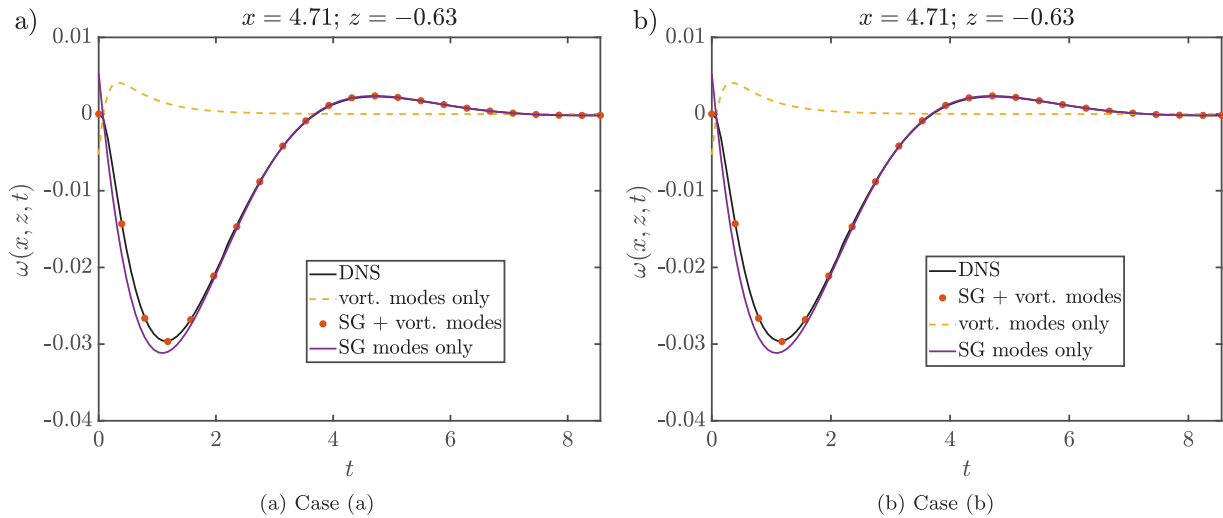

Fig. 7. Vorticity, at a location in space ($x = 4.71, z = -0.63$) close to the interface, plotted as a function of time for the cases (a) and (b), respectively. Here, the vertical axis is the non-dimensional vorticity ($\omega^*/\sqrt{g^* k^*}$) and the horizontal axis the non-dimensional time ($t^* \sqrt{g^* k^*}$).

perturbation vorticity field at large depth seen in DNS, the approximation becomes quite inaccurate close to the free-surface $z = 0$. Here at early time $t > 0$, the contribution from both SG and vorticity modes nearly (but not entirely) cancel each other, producing a (boundary) vorticity layer adjacent to the free surface (see DNS signal in black). The overall conclusion is that in order to obtain a good match with the DNS vorticity field close to the free surface, we require contributions from both sets of modes. These conclusions remain unaltered when we refer back to case (a) in Table 2, which corresponds to zero vorticity initial condition. Observing the DNS signal in Fig. 6(a), we note that the perturbation vorticity field in this case is only adjacent the free surface (and zero in the bulk liquid). Expressing this vorticity field near the free-surface accurately requires contributions from vorticity and SG modes consistent with observations by Prosperetti (1976).

We had mentioned earlier (Lamb, 1932; Prosperetti, 1976) that in the unstratified, infinite depth limit the spectrum has an additional continuous part and that these continuous spectrum (CS) modes have an oscillatory variation in the z direction. Such behaviour may also

been seen among a subset of the discrete spectrum modes in the finite depth case as we argue below. In dimensional variables, the diffusion equation governing the perturbation vorticity field admits solutions of the form $\exp\left[z\left(k^2 + \tilde{s}/\nu^{(\mathcal{L})}\right)^{1/2}\right]$ with $\mathrm{Re}\left(k^2 + \tilde{s}/\nu^{(\mathcal{L})}\right)^{1/2} > 0, \; z < 0$. For the countably infinite set of vorticity modes in Fig. 4(a) for which $\tilde{s}$ is real, negative and which additionally satisfy $|\tilde{s}| \gg \nu^{(\mathcal{L})} k^2$, such a solution to the diffusion equation becomes an oscillatory functions of z behaving as $\sim \exp\left(z\sqrt{\tilde{s}/\nu^{(\mathcal{L})}}\right)$, $\tilde{s}$ being real and negative. For comparison, the contribution from the CS modes in the infinite depth case (from the branch cut) are also plotted in Figs. 6(a) and 6(b). We observe that these are indistinguishable from the contribution due to the vorticity modes in the finite depth case. Note that the non-dimensional depth H for case (a) and (b) in Table 2 is finite but large.

The acronym NMA in Figs. 5(a) and 5(b) represents what we term as the normal mode approximation (eqn. 3.3 also used earlier in Farsoiya et al. (2017)). This is an approximation based on the observation that
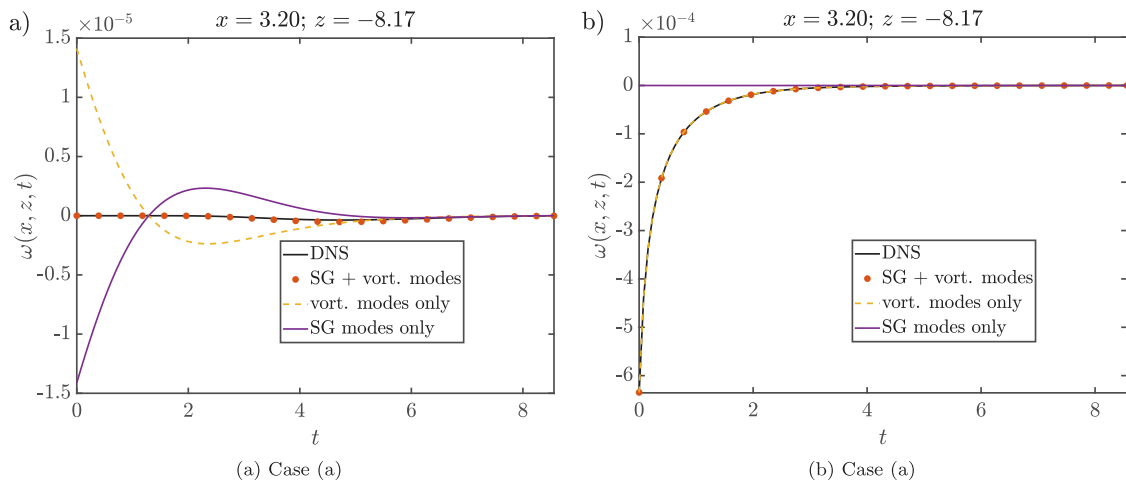
Fig. 8. Vorticity, at a location in space ($x = 4.71, z = -8.17$) deep inside the pool, plotted as a function of time for the cases (a) and (b), respectively. Here, the vertical axis is the non-dimensional vorticity ($\omega^*/\sqrt{g^* k^*}$) and the horizontal axis the non-dimensional time ($t^* \sqrt{g^* k^*}$). (For interpretation of the references to colour in this figure legend, the reader is referred to the web version of this article.)
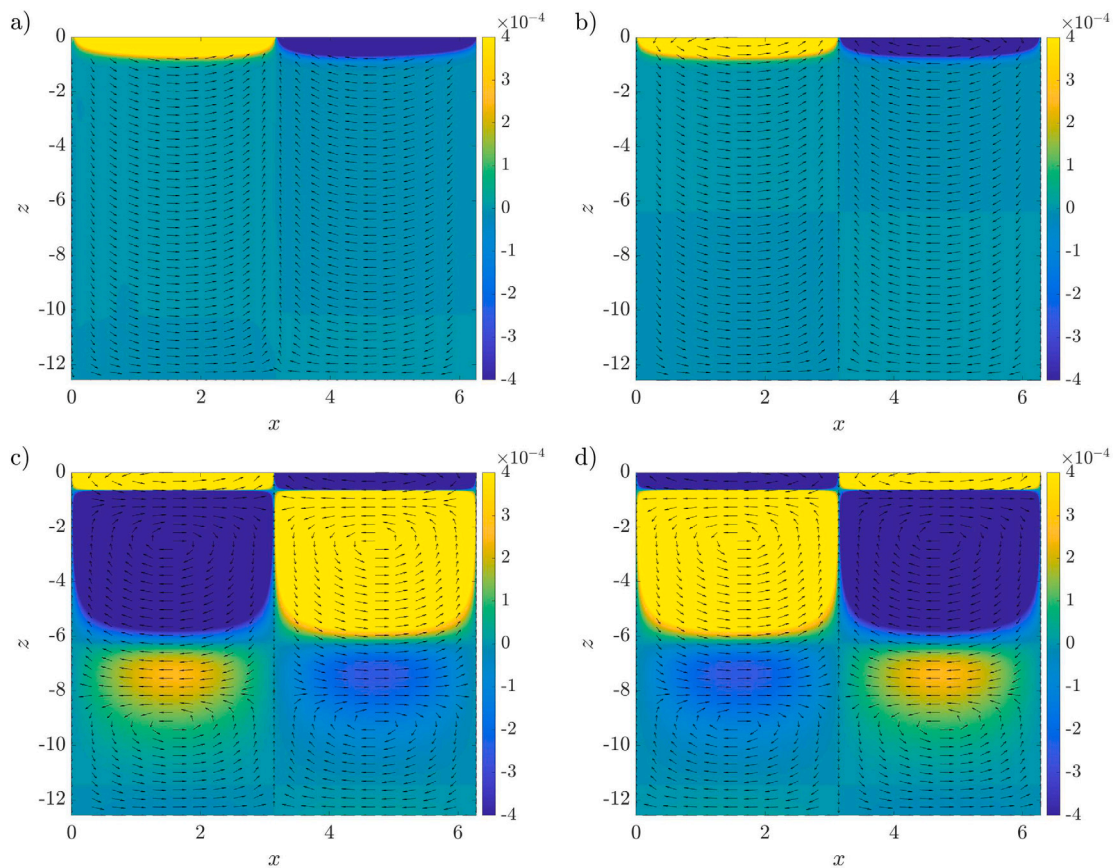
Fig. 9. Vorticity contours corresponding to case (a) at time $t = 0.079$ from: (a) DNS (b) Total IVP (SG + visc. modes) (c) IVP (SG modes only) (d) IVP (vort. modes only). The arrows at different locations indicate the instantaneous velocity at these locations. The horizontal and vertical axes are non-dimensional x ($= x^* k^*$) and z ($= z^* k^*$) coordinates, respectively.

there are only two SG modes in the spectrum. This may be used to satisfy the free surface initial conditions $a(0) = a_0$ and $\dot{a}(0) = 0$, leading to a predictive expression for the free surface evolution viz. $\frac{a(t)}{a(0)} = \frac{1}{s_1 - s_2} \left(s_1 \exp s_2 t - s_2 \exp s_1 t \right)$, where s_1, s_2 are the two complex conjugate pair of SG modes in Fig. 4(a). We note that by construction the NMA satisfies the initial conditions at the free surface; although it shows a rather large mismatch with the DNS signal in Figs. 5(a) and 5(b), at intermediate time. The curves labelled as 'SG + vort. modes'

in these figs. represent the solution to the complete IVP taking into account contributions from both sets of modes. Expectedly, we note the excellent agreement of this with DNS. Returning to our observation of Figs. 5(a) and 5(b) being identical, we note that this is an outcome of the vorticity perturbation being placed sufficiently deep. As a consequence, this perturbation vorticity at large depth (which is well described by a linear superposition of the vorticity modes only), evolves purely diffusively nearly independent of the evolution of the transient
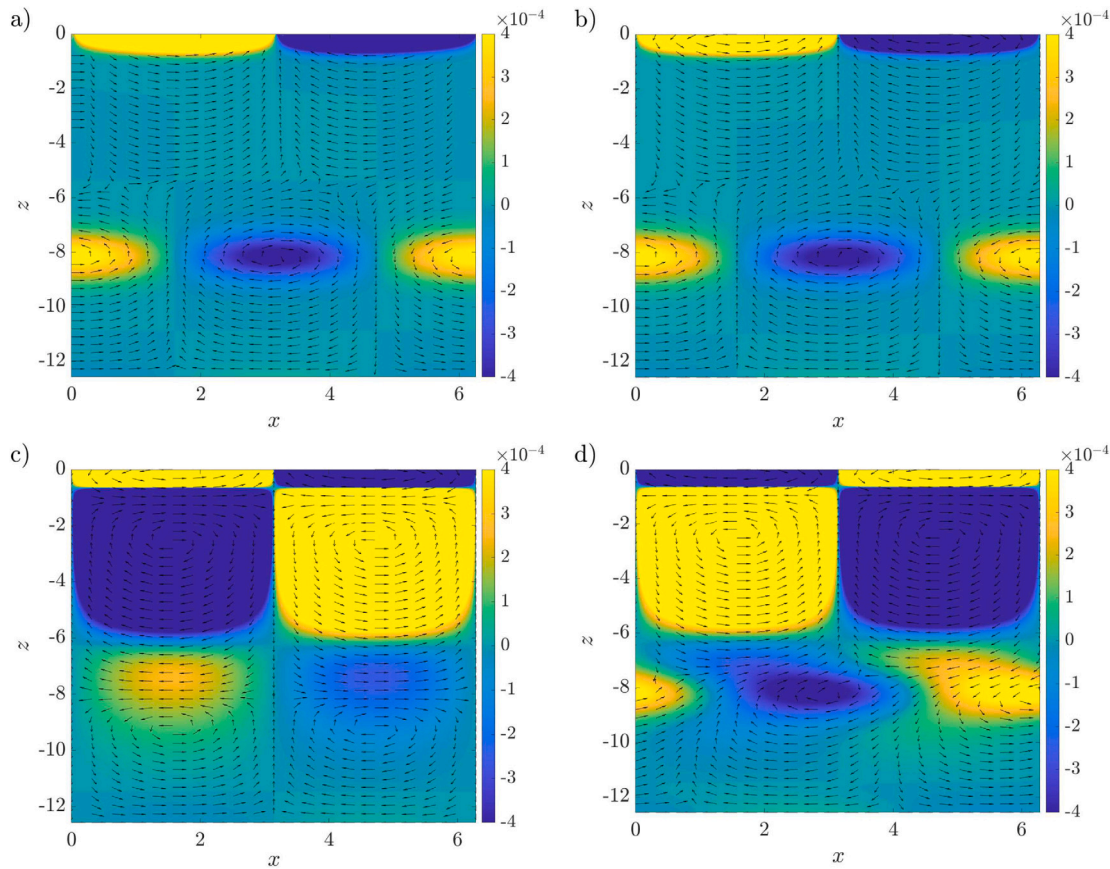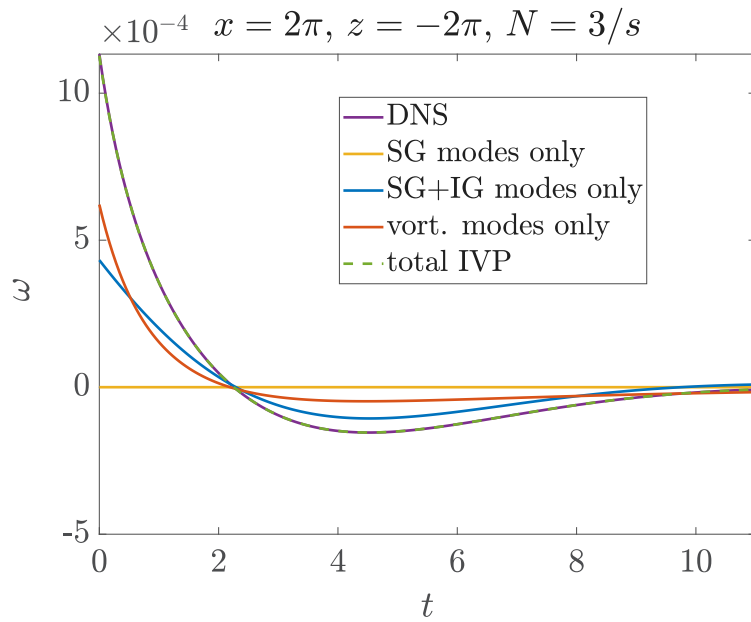
Fig. 10. Vorticity contours corresponding to case (b) at time $t = 0.079$ from: (a) DNS (b) Total IVP (SG + visc. modes) (c) IVP (SG modes only) (d) IVP (vort. modes only). The horizontal and vertical axes are non-dimensional in the same way as Fig. 9.

vorticity layer generated at the free-surface. This behaviour is to be contrasted with the observations of Prosperetti and Cortelezzi (1982) where surface waves produced due to a submerged vortex filament (extending along the y direction) and an initial flat free-surface was studied analytically. In contrast to our present study where a single Fourier mode of wave number k is excited along the x-direction (both in case (a) and case (b) in Table 2), the initial condition of Prosperetti and Cortelezzi (1982) excites a continuous spectrum of wavenumbers k at $t = 0$. Waves at the free surface are observed subsequently due to the presence of the vortex filament in the pool below (see figs. 1 and 2 in Prosperetti and Cortelezzi (1982)). The submergence depth of the vortex filament in their case was 0.1 and 0.01 cms respectively, both of which are significantly smaller than the wavelength of the slowest capillary–gravity surface wave excited in their system. In contrast, our submergence depth of the Gaussian patch in case (b) (1.3 cm) exceeds the wavelength of the surface wave excited at $t = 0$.

Figs. 7(a) and 7(b) show the vorticity at a particular spatial location $x(= 4.71)$ and $z(= -0.63)$, plotted as a function of time for cases (a) and (b) respectively of Table 2. Note that the vertical coordinate of this location is quite close to the free-surface and thus we expect the vorticity field in case (a) and case (b) to look similar as is easily verified from the two figures. Considering the contribution of SG modes once again leads to slightly erroneous results at initial times. When the depth is chosen to be farther from the free-surface, as in Figs. 8(a) and 8(b), a clear difference is seen in the temporal evolution of the perturbation vorticity. For case (a) described in Fig. 8(a), at $z = -8.17$ the perturbation vorticity field is effectively zero at all time and this is achieved analytically only by taking the mutually cancelling contributions from the SG modes (yellow) and the vorticity modes (purple). In contrast, for case (b) in Fig. 8(b) the perturbation vorticity field is markedly different from zero at this depth (due to the initial Gaussian vorticity

perturbation). As expected, the burden of describing the time variation of this vorticity is taken up solely by the vorticity modes without any contribution from the SG modes.

A global picture of the perturbation vorticity as well as flow field, at early time $t(= 0.079)$ once again for cases (a) and (b) in Table 2 are provided in Fig. 9, panels (a)–(d) and Fig. 10, panels (a)–(d) respectively. In these figures, the horizontal axis spans one wavelength and the vertical axis spans two wavelengths (in non-dimensional sense). Panels (a) and (b) in Fig. 9 indicate a good agreement between DNS results and IVP predictions. Panels (c) and (d) in the same figure show flow structures due to contributions from SG modes and vorticity modes, respectively, nearly cancel each other leading to what is observed in the upper panels. A similar behaviour is observed in Fig. 10, panels (a)–(d), representing case (b) in Table 2. Note that in contrast to Fig. 9, panels (c) and (d) in this figure are visibly asymmetrical and the contribution from vorticity modes resolves almost entirely, the initial perturbation vorticity. Turning now to case (c) in Table 2, which represents a stratified case (Brunt-Vaisala frequency $N = 3$ s^{-1}) with only vorticity initial perturbation. Fig. 11 depicts the vorticity at a particular location $x = 2\pi, z = -2\pi$. It is seen from this figure that the initial vorticity perturbation has projections on both vorticity as well as internal gravity modes (IG). Note that in this case, we do not impose any free-surface disturbance and thus the SG modes are never excited. It is seen that the vorticity at this location changes sign going to zero at large time. In order to obtain the vorticity signal seen in DNS, contributions from both SG as well as IG modes are found to be equally important. Figs. 11(b) and 11(c) show the perturbation vorticity field at $t = 0$ and $t = 3.91$ respectively. Once again, we see the same qualitative features as 11(a) viz. that in order to match the DNS vorticity profile accurately, contributions from both IG and vorticity modes are to be taken into account. Finally, Fig. 12 shows the effect of

(a) Vorticity $\omega(x, z, t)$
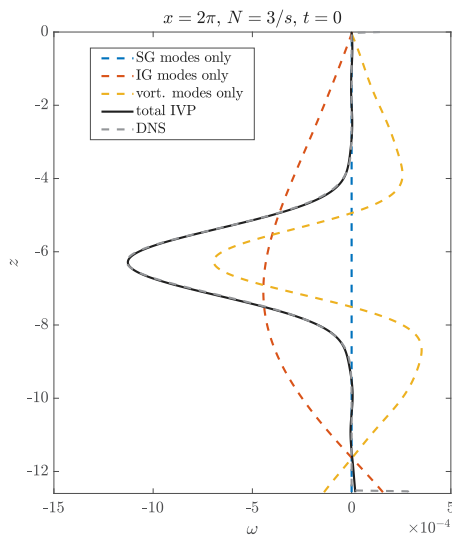
(b) $t = 0$
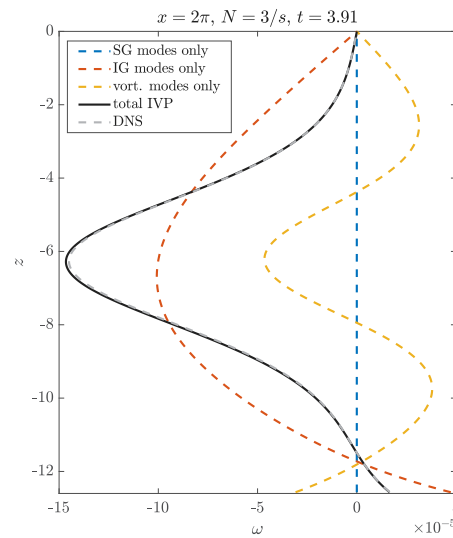
(c) $t = 3.91$

Fig. 11. Vorticity plots corresponding to case (c) in Table 2 at $t = 0$ from DNS versus analytical predictions: Panel (a) vorticity vs. time, panels (b) and (c) vorticity vs. z at $t = 0$ and $t = 3.91$.

increasing stratification (case (d) compared to case (c)) on the evolution of the vorticity perturbation as a function of time. Due to increased stratification in case (d), a significant oscillatory response in the local vorticity value is seen for case (d).

5. Conclusions

In this study, we have solved the linearised initial-value problem (IVP) for a stratified pool of viscous liquid, corresponding to free-surface, vorticity and density initial conditions. The temporal spectrum has been studied carefully in various limits (viscous versus inviscid, stratified versus unstratified and finite versus infinite depth) relating this to the response predicted from our analytical solution to the IVP. We have compared some of our analytical predictions against Direct Numerical Simulations using the open source code Basilisk (Popinet,

2014), obtaining excellent agreement in all cases. The analytical solutions permits individual examination of various parts of the spectrum and their respective contributions.

In the unstratified, finite depth limit, we find that

- the countably infinite set of vorticity modes are crucial for satisfying initial conditions as well as for describing any perturbation vorticity imposed at depths, where the contribution from the surface-gravity (SG) modes is effectively zero,
- when this perturbation vorticity field (Gaussian) is chosen to be at sufficient depth, this field evolves nearly independently of the transient vorticity field produced at the free-surface,
- consequently, we find that when the perturbation vorticity field is introduced at large depth, it produces a negligible surface signature, but nevertheless requires the vorticity modes to describe its temporal evolution,
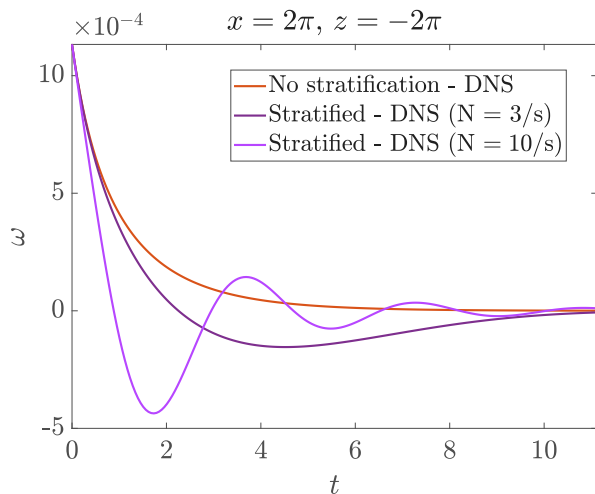
Fig. 12. Vorticity vs. time corresponding to cases (c) and (d) in Table 2 from DNS.

- in contrast, the vorticity at the free surface has near equal contributions from both SG as well as vorticity modes and neglecting any of these leads to a large error,
- in the infinite depth limit, the contribution from the continuous spectrum modes to the time evolution of the vorticity field is found to be numerically indistinguishable from that of the countably infinite, vorticity modes in the finite, but large depth case.

Considering a stratified viscous pool of liquid without any initial surface perturbation and an initial Gaussian shaped localised perturbation vorticity patch, we find that

- the time evolution of the patch has nearly equal contributions from the vorticity and the internal gravity modes.

Our study with a careful comparison of the temporal spectrum in each case to the IVP response, extends previous results for an unstratified pool due to Prosperetti (1976) and Prosperetti and Cortelezzi (1982) and to the viscous case for a stratified pool (Yih, 1960). Several analytical predictions are tested against fully nonlinear, numerical simulations obtaining excellent agreement in all cases. This study will have several applications in studies of thermo-capillary instabilities on a liquid layer.

Declaration of competing interest

The authors declare that they have no known competing financial interests or personal relationships that could have appeared to influence the work reported in this paper.

Data availability

I have shared the code as supplementary material.

Appendix A. Supplementary data

Supplementary material related to this article can be found online at https://doi.org/10.1016/j.ijmultiphaseflow.2023.104592.

References

Antoon van Hooft, J., 2018. Damping Internal Waves In a stratified fluid. http://basilisk.fr/sandbox/Antoonvh/internalwacesMGdamping.c.
Antuono, M., Colagrossi, A., 2013. The damping of viscous gravity waves. Wave Motion 50 (2), 197–209.
Basak, S., Farsoiya, P.K., Dasgupta, R., 2021. Jetting in finite-amplitude, free, capillary-gravity waves. J. Fluid Mech. 909, A3.
Basset, A.B., 1888. A Treatise on Hydrodynamics: With Numerous Examples, Vol. 2. Deighton, Bell and Company.
Berger, S., 1988. Initial-value stability analysis of a liquid jet. SIAM J. Appl. Math. 48 (5), 973–991.
Beyer, J., Friedrich, R., 1995. Faraday instability: linear analysis for viscous fluids. Phys. Rev. E 51 (2), 1162.
Cauchy, A., 1827. Théorie de la propagation des ondes a la surface d'un fluide pesant d'une profondeur indéfinie Note XIX Sur les fonctions réciproques. In: Mémoires Présentés par Divers Savants á l'Académie Royale des Sciences de l'Institut de France et Imprimés par son Ordre. Sciences Mathématiques et Physiques, Vol. 1.
Cerda, E., Tirapegui, E., 1997. Faraday's instability for viscous fluids. Phys. Rev. Lett. 78 (5), 859.
Cerda, E., Tirapegui, E., 1998. Faraday's instability in viscous fluid. J. Fluid Mech. 368, 195–228.
Chandrasekhar, S., 1981. Hydrodynamic and Hydromagnetic Stability. Dover, New York.
Cortelezzi, L., Prosperetti, A., 1981. Small-amplitude waves on the surface of a layer of a viscous liquid. Quart. Appl. Math. 38 (4), 375–389.
Craik, A.D.D., 2004. Annu. Rev. Fluid Mech. 36, 1–28.
Debnath, L., 1994. Nonlinear Water Waves. Academic Press.
Debnath, L., Guha, U.B., 1989. The Cauchy-Poisson problem in an inviscid stratified liquid. Appl. Math. Lett. 2 (4), 337–340.
Denner, F., 2016. Frequency dispersion of small-amplitude capillary waves in viscous fluids. Phys. Rev. E 94 (2), 023110.
Ellingsen, S.Å., 2014. Initial surface disturbance on a shear current: The Cauchy-Poisson problem with a twist. Phys. Fluids 26 (8), 082104.
Farsoiya, P.K., Magdelaine, Q., Antkowiak, A., Popinet, S., Deike, L., 2023. Direct numerical simulations of bubble-mediated gas transfer and dissolution in quiescent and turbulent flows. J. Fluid Mech. 954, A29.
Farsoiya, P.K., Mayya, Y., Dasgupta, R., 2017. Axisymmetric viscous interfacial oscillations–theory and simulations. J. Fluid Mech. 826, 797–818.
Farsoiya, P.K., Roy, A., Dasgupta, R., 2020. Azimuthal capillary waves on a hollow filament–the discrete and the continuous spectrum. J. Fluid Mech. 883.
Felderhof, B., 2006. Dynamics of an interface with adsorption layer between two fluids. Phys. Fluids 18 (11), 112103.
Foster, M., Saffman, P., 1970. The drag of a body moving transversely in a confined stratified fluid. J. Fluid Mech. 43 (2), 407–418.
Ghosh, P., Basu, U., Mandal, B., 2000. Waves due to initial disturbances at the inertial surface in a stratified fluid of finite depth. Int. J. Math. Math. Sci. 24 (4), 265–276.
Gurski, K.F., Kollár, R., Pego, R., 2004. Slow damping of internal waves in a stably stratified fluid. Proc. R. Soc. Lond. Ser. A Math. Phys. Eng. Sci. 460 (2044), 977–994.
Harrison, W., 1908. The influence of viscosity on the oscillations of superposed fluids. Proc. Lond. Math. Soc. 2 (1), 396–405.
Inc., W.R., 2022. Mathematica, Version 13.2. Champaign, IL.
Johnson, R.S., 1997. A Modern Introduction to the Mathematical Theory of Water Waves, 19. Cambridge University Press.
Kayal, L., Basak, S., Dasgupta, R., 2022. Dimples, jets and self-similarity in nonlinear capillary waves. J. Fluid Mech. 951, A26.
Lamb, H., 1932. Hydrodynamics. Cambridge Univ Press.
Lighthill, J., 1996. Internal waves and related initial-value problems. Dyn. Atmos. Oceans 23 (1–4), 3–17.
Lucassen, J., 1968. Longitudinal capillary waves. part 1.—theory. Trans. Faraday Soc. 64, 2221–2229.
Lucassen-Reynders, E., Lucassen, J., 1970. Properties of capillary waves. Adv. Colloid Interface Sci. 2 (4), 347–395.
Miles, J.W., 1968. The Cauchy-Poisson problem for a viscous liquid. J. Fluid Mech. 34 (02), 359–370.
Patankar, S., Basak, S., Dasgupta, R., 2022. Dynamic stabilisation of Rayleigh–Plateau modes on a liquid cylinder. J. Fluid Mech. 946, A2.
Poisson, S., 1818. Memoire sur la theories des ondes. Mem. Acad. Roy. Sci. Inst. France (2) 1 (18), 16.
Popinet, S., 2014. Basilisk. http://basilisk.fr.
Prosperetti, A., 1976. Viscous effects on small-amplitude surface waves. Phys. Fluids (1958-1988) 19 (2), 195–203.

Prosperetti, A., 1980. Normal-mode analysis for the oscillations of a viscous-liquid drop in an immiscible liquid. J. Méc. 19 (1), 149–182.

Prosperetti, A., 1981. Motion of two superposed viscous fluids. Phys. Fluids (1958-1988) 24 (7), 1217–1223.

Prosperetti, A., Cortelezzi, L., 1982. Small-amplitude waves produced by a submerged vorticity distribution on the surface of a viscous liquid. Phys. Fluids 25 (12), 2188–2192.

Rednikov, A.Y., Colinet, P., Velarde, M.G., Legros, J.C., 2000. Rayleigh–Marangoni oscillatory instability in a horizontal liquid layer heated from above: coupling and mode mixing of internal and surface dilational waves. J. Fluid Mech. 405, 57–77.

Riley, K.F., Hobson, M.P., Bence, S.J., 2006. Mathematical methods for physics and engineering third edition paperback set. In: Mathematical Methods for Physics and Engineering-3rd Edition. p. 1362.

Rollins, D., Debnath, L., 1992. The Cauchy-Poisson waves in an inviscid rotating stratified liquid. Int. J. Non-Linear Mech. 27 (3), 405–412.

Sanjay, V., Sen, U., Kant, P., Lohse, D., 2022. Taylor–Culick retractions and the influence of the surroundings. J. Fluid Mech. 948, A14.

Shardt, O., Masoud, H., Stone, H.A., 2016. Oscillatory Marangoni flows with inertia. J. Fluid Mech. 803, 94–118.

Shen, L., Denner, F., Morgan, N., van Wachem, B., Dini, D., 2017. Marangoni effect on small-amplitude capillary waves in viscous fluids. Phys. Rev. E 96 (5), 053110.

Shen, L., Denner, F., Morgan, N., van Wachem, B., Dini, D., 2018. Capillary waves with surface viscosity. J. Fluid Mech. 847, 644–663.

Simakov, S.T., 1993. Initial and boundary value problems of internal gravity waves. J. Fluid Mech. 248, 55–65.

Singh, M., Farsoiya, P.K., Dasgupta, R., 2019. Test cases for comparison of two interfacial solvers. Int. J. Multiph. Flow. 115, 75–92.

Sutherland, B.R., 2010. Internal Gravity Waves. Cambridge University Press.

Thomas, N., Stevenson, T., 1972. A similarity solution for viscous internal waves. J. Fluid Mech. 54 (3), 495–506.

Tyvand, P.A., Mulstad, C., Bestehorn, M., 2021a. A nonlinear impulsive Cauchy–Poisson problem. Part 1. Eulerian description. J. Fluid Mech. 906.

Tyvand, P.A., Mulstad, C., Bestehorn, M., 2021b. A nonlinear impulsive Cauchy–Poisson problem. Part 2. Lagrangian description. J. Fluid Mech. 906.

Vallis, G.K., 2017. Atmospheric and Oceanic Fluid Dynamics. Cambridge University Press.

Vartdal, M., Osnes, A.N., 2019. Linear motion of multiple superposed viscous fluids. Phys. Rev. E 99 (4), 043104.

Voisin, B., 1991. Internal wave generation in uniformly stratified fluids. Part 1. Green's function and point sources. J. Fluid Mech. 231, 439–480.

Voisin, B., 1994. Internal wave generation in uniformly stratified fluids. Part 2. Moving point sources. J. Fluid Mech. 261, 333–374.

Wolfram, S., 2013. Mathematica, Version 8. Wolfram research, Inc., 23.

Wu, T.Y.-T., Mei, C., 1967. Two-dimensional gravity waves in a stratified ocean. Phys. Fluids 10 (3), 482–486.

Yih, C.-S., 1960. Gravity waves in a stratified fluid. J. Fluid Mech. 8 (4), 481–508.